Curvature Regularization near Contacts with Stretched Elastic Tubes

Bhargav Rallabandi,[1,*] Joel Marthelot,[2,4] Etienne Jambon-Puillet,[2] P.-T. Brun,[2] and Jens Eggers[3,†]
[1]Department of Mechanical Engineering, University of California, Riverside, California 92521, USA
[2]Department of Chemical and Biological Engineering, Princeton University, Princeton, New Jersey 08544, USA
[3]School of Mathematics, University of Bristol, Fry Building, Bristol BS8 1UG, United Kingdom
[4]Aix-Marseille University, CNRS, IUSTI, Marseille 13013, France

(Received 22 February 2019; revised manuscript received 25 August 2019; published 17 October 2019)

Inserting a rigid object into a soft elastic tube produces conformal contact between the two, resulting in contact lines. The curvature of the tube walls near these contact lines is often large and is typically regularized by the finite bending rigidity of the tube. Here, it is demonstrated using experiments and a Föppl–von Kármán–like theory that a second, independent, mechanism of curvature regularization occurs when the tube is axially stretched. In contrast with the effects of finite bending rigidity, the radius of curvature obtained increases with the applied stretching force and decreases with sheet thickness. The dependence of the curvature on a suitably rescaled stretching force is found to be universal, independent of the shape of the intruder, and results from an interplay between the longitudinal stresses due to the applied stretch and hoop stresses characteristic of curved geometry. These results suggest that curvature measurements can be used to infer the mechanical properties of stretched tubular structures.

DOI: 10.1103/PhysRevLett.123.168002

The mechanics of thin sheets (or plates) are determined by the interplay between bending and stretching [1–3]. As the sheet is deformed from its rest state, it bends out of its plane, but it must also stretch in its own plane in order to accommodate its new shape. Bending rigidity B prevents the sheet from turning too sharp a corner, so it is the ratio of B to some other scale—such as one involving interfacial tension [4–6], an external pressure [3,7], or gravity [8,9]—that sets the size of the smallest ridge [1] or the wavelength of wrinkles [2]. Shells are sheets with curved rest shapes, such as a sphere or a cylinder. This introduces nontrivial differential geometry as well as extra length scales (e.g., the rest radius of a cylinder) that govern the buckling [10,11] and wrinkling [7,12] of shells (see also [13]). The competition of bending and stretching energies also determines the geometry of crystalline closed membranes [14], multicomponent vesicles (line energies also contribute) [15,16], pinched tubes [17], and indented microtubules [18].

In this Letter we discuss a mechanism of generating out-of-plane curvature through externally applied in-plane forces, entirely *independent* of bending energy. We will focus on soft cylindrical shells (i.e., tubes), which introduces a high degree of anisotropy, as they are curved in the azimuthal direction but are flat along the axis. In particular, an object can be confined inside a tube without applying any external force, in which case a sharp corner forms at the geometrical intersection between the cylinder and the intruder [19]. We will show that the subsequent application of an axial stretching force F regularizes this corner due to a combination of the resulting axial strain and geometric constraints, even without invoking any bending rigidity. The resulting length scale depends on the external force and bears some resemblance with the "elastic capillary length" introduced previously in the context of wrinkling [3,7].

We consider a thin-walled elastic tube that in its undeformed reference configuration has a cylindrical shape with radius a, into which is introduced a larger axisymmetric intruder of maximum radius $R_0 > a$ [Fig. 1(a)] [19–21]. The coordinate s measures the arclength in the reference state [Fig. 1(a)] and thus labels material points [13]. The tube may additionally be acted on by a traction (force per area) $\sigma(s)$ along its surface and forces per length $\pm\mathbf{f}$ on its circular rims [Fig. 1(a)].

The external forces and the intruder (which contacts the tube over a finite area) together deform the tube walls. Figures 1(b)–1(e) show images of a spherical intruder (304 stainless steel ball bearing, radius $R_0 = 6.35$ mm) in a commercial cylindrical latex balloon (rest radius $a = 3.25$ mm, thickness $b = 320$ μm), clamped on one side and attached to the load cell of a universal testing machine (Instron) on the other. We record the tensile force F as the cylindrical tube is stretched along its axis. The shape of the deformed tube is imaged with a high-resolution camera. Experiments with nonspherical intruders are discussed near the end of this Letter.

As is evident in Figs. 1(b)–1(e), stretching the tube increases the length scale over which the tube relaxes to its cylindrical shape. In particular, in the absence of an applied stretch, a kink forms at the geometric intersection of the intruder with the undeformed tube, and is gradually smoothed as the tube is stretched. Simultaneously, the contact area between the soft tube and the rigid intruder

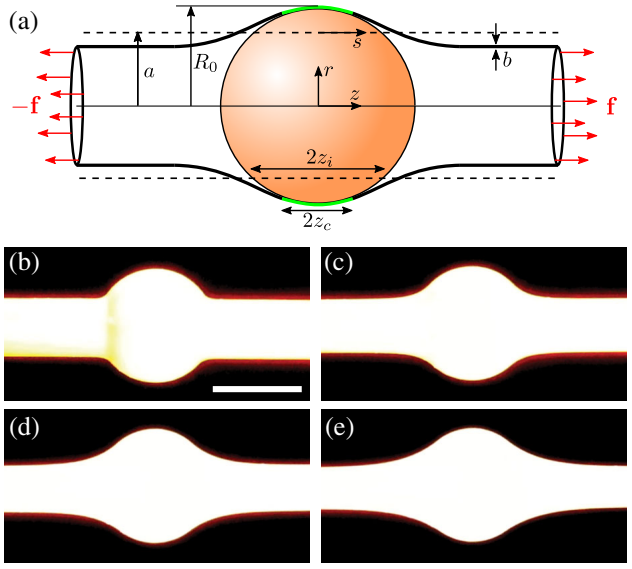

FIG. 1. (a) Sketch of the setup showing an axisymmetric intruder in a tube (solid lines) that is cylindrical (radius a) in its undeformed reference configuration (dashed lines). The tube is stretched by applying equal and opposite forces per length of magnitude $f = F/(2\pi a)$ at the tube ends. The arclength coordinate s in the undeformed configuration is a material label. The intersection of the undeformed tube and the intruder defines a geometric intersection length $2z_i$ while the region of contact (highlighted in green) has axial extent $2z_c$. (b)–(e) Experimental pictures of the shape of the tube of radius $a = 3.25$ mm around an intruder of radius $R_0 = 6.35$ mm for increasing values of the applied force F. Scale bar is 10 mm.

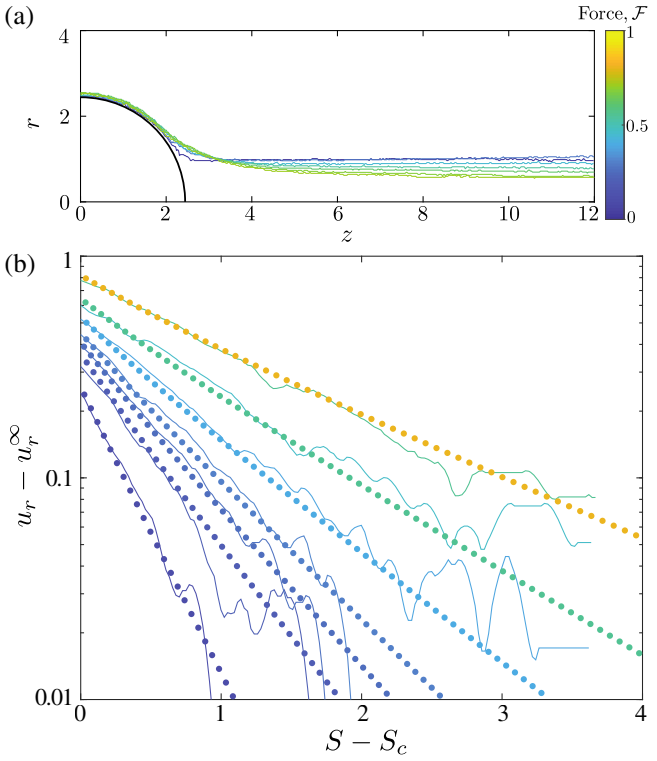

FIG. 2. (a) Experimental profiles obtained with a spherical intruders of dimensional radius $R_0/a = 2.44$. The dimensionless force $\mathcal{F}$ is coded in color. (b) Exponential decay of the radial displacement $u_r - u_r^\infty$ with distance from the contact point $S - S_c$ for increasing dimensionless stretching forces. Solid lines are experiments for $\mathcal{F} = 0.13$, 0.22, 0.27, 0.32, 0.38, 0.46, and 0.55, and symbols are theoretical predictions for $\mathcal{F} = 0.1$, 0.2, 0.25, 0.3, 0.4, 0.55, and 0.8.

decreases. We show that this curvature regularization is a consequence of axial strains of the tube being coupled to radial stresses through cylindrical geometry, independent of bending rigidity.

We model an intruder inside a cylindrical tube using a nonlinear shell theory analogous to the Föppl–von Kármán (FvK) theory for plates [22], applicable to small strains and moderate rotations of the elastic tube surface. In this theory, out-of-plane deformations and in-plane stretching are treated within linear elasticity, but stretching is coupled geometrically to potentially large deformations of the shell from its rest state, resulting in a strongly *nonlinear* theory. Defining the displacement $\mathbf{u}(s) = u_r(s)\mathbf{e}_r + u_z(s)\mathbf{e}_z$ and following the shell theory developed in Audoly and Pomeau [13] (p. 447), the deformation of the tube is governed by the stress balance

$$\frac{d(N_s\mathbf{t})}{ds} - \frac{N_\theta}{a}\mathbf{e}_r + \sigma = \mathbf{0}, \tag{1}$$

where $\mathbf{t}(s) = u_r'(s)\mathbf{e}_r + \mathbf{e}_z$ approximates the tangent to the deformed surface (primes denotes a derivative with respect to the argument) and $N_s(s)$ and $N_\theta(s)$ are, respectively, the axial and azimuthal diagonal elements of the in-plane stress tensor (with units of force per length). In particular, N_θ is the hoop stress characteristic of cylindrical geometry. The bending rigidity of the tube walls has been neglected in (1) but will be reintroduced later in the discussion. The radial component of (1) has the form of a membrane equation [22], where the second term resembles the capillary pressure of a fluid cylinder [23], with the hoop stress N_θ playing the role of surface tension. Expanding for small wall thickness $b \ll a$ (Young's modulus E, Poisson's ratio ν), one finds $N_s = (Eb/1-\nu^2)[u_z' + \frac{1}{2}(u_r')^2 + \nu(u_r/a)]$ and $N_\theta = (Eb/1-\nu^2)[(u_r/a) + \nu(u_z' + \frac{1}{2}(u_r')^2)]$ [13]. In the limit $a \to \infty$ one recovers the standard plate equations, and the hoop stress drops out of the description. We focus on the case relevant to our experiments, viz. no tractions act on the noncontacting part of the tube surface and axial stretching forces act at the tube ends [$\pm\mathbf{f} = \pm\mathbf{e}_z f$, $f = F/(2\pi a)$]; cf. Fig. 1(a).

Figure 2(a) presents the shapes of such tubes obtained experimentally. The shapes are color coded using the value of the dimensionless stretching force defined by $\mathcal{F} \equiv F/(2\pi Eab)$ where $E = 1.29$ MPa is the Young modulus of the latex tube. The shape of the tube depends both on the shape of the intruder, given by $r = R(z)$, and the applied

stretching force per circumference f. In experiments, it is natural to measure the radial displacement as a function of the *deformed* arclength S instead of the undeformed coordinate s. The tube loses contact with the intruder at two contact lines at $s = \pm s_c$ ($S = \pm S_c$; $z = \pm z_c$) that depend on F. Our experimental data suggest an exponential relaxation of the radial displacement $u_r - u_r^\infty$ [where $u_r^\infty = u_r(s \to \infty)$] with distance from the contact point $S - S_c$ [lines in Fig. 2(b)] over a length scale that increases with the applied force.

To predict this relaxation length theoretically, it is convenient to first rescale all lengths by a and define $\tilde{s} = s/a$, $\tilde{s}_c = s_c/a$, $\tilde{\mathbf{u}}(\tilde{s}) = \mathbf{u}(s)/a$, $\tilde{R}_0 = R_0/a$ etc., where the contact line location $\tilde{s}_c$ must be found as part of the solution. Below, we consider objects symmetric about $s = z = 0$ and focus on $s \geq 0$, although we later show that our experimental results are robust against this assumption. Dropping tilde accents for convenience, the dimensionless form of (1) over the noncontacting part of the tube surface ($s > s_c$), where $\sigma = \mathbf{0}$, is

$$\mathcal{F} u_r'' - u_r - \nu\mathcal{F} = 0, \tag{2a}$$

$$u_z' + \frac{1}{2}(u_r')^2 + \nu u_r = (1 - \nu^2)\mathcal{F}, \tag{2b}$$

where we have utilized equilibrium at the end of the tube [in dimensional terms, $N_s(s \to \infty) = F/(2\pi a)$]. The system (2) admits the general decaying solutions

$$u_r(s > s_c) = -\nu\mathcal{F} + Ce^{-(s-s_c)/\sqrt{\mathcal{F}}}, \tag{3a}$$

$$u_z(s > s_c) = D + (s - s_c)\mathcal{F} + \nu C\sqrt{\mathcal{F}}e^{-(s-s_c)/\sqrt{\mathcal{F}}} + \frac{C^2}{4\sqrt{\mathcal{F}}}e^{-2(s-s_c)/\sqrt{\mathcal{F}}}, \tag{3b}$$

where C, D, and s_c are yet-undetermined constants. Thus, according to (3a), the tube relaxes from the contact point over a dimensionless length scale $\sqrt{\mathcal{F}}$, to a cylindrical shape of radius $1 - \nu\mathcal{F}$. This length scale is analogous to the "elastic capillary length" for spherical shells [3,7], but where instead of the intrinsic pressure N_θ/a produced by the applied force, the pressure is imposed from the outside.

The unknown constants in (3) are determined by the solution in the contact region ($0 \leq s \leq s_c$). Since $z(s) = s + u_z(s)$ is the axial coordinate of a material point s in the deformed state, contact is defined by the geometric constraint $\delta[z(s)] \equiv R[z(s)] - 1 = u_r(s)$. Then, continuity of displacement and tangential stress leads to the condition (see Supplemental Material [24])

$$\delta' = \frac{-2\sqrt{\mathcal{F}}(\delta + \mathcal{F}\nu)}{\mathcal{F}[2 - 4\delta\nu + \mathcal{F}(2 - 3\nu^2)] - \delta^2} \quad \text{at } z = z_c, \tag{4}$$

which is an algebraic equation in z whose solution determines the axial location z_c of the contact point. The constraint of contact is enforced physically by a contact stress $\sigma(s)$ exerted by the intruder. Assuming negligible friction, $\sigma(s) = p_c(s)\mathbf{n}$ for $|s| < s_c$, where $\mathbf{n}(s) = \mathbf{e}_r - u_r'(s)\mathbf{e}_z$ approximates the normal to the surface. Substituting this expression for σ into (1) and using the geometric constraint leads to a single differential equation for $u_z(s)$, which we integrate from $s = 0$ [using $u_z(0) = 0$], until the solution satisfies $z_c = s_c + u_z(s_c)$, thus identifying s_c (see Supplementary Material [24]). This procedure self-consistently determines $u_r(s)$, $u_z(s)$, the contact pressure $p_c(s)$, the contact point s_c and the coefficients C and D through the displacement and stress-continuity relations, completing the solution to the problem along the entire length of the tube. The dimensionless deformed arclength is then computed as $S(s) = \int_0^s \sqrt{[1 + u_z'(\tau)]^2 + [u_r'(\tau)]^2}\, d\tau$.

Typical numerical results for a spherical $R(z)$ are plotted in Fig. 3(a), showing both the shape of the tube surface and the location of the contact point for different $\mathcal{F}$. As $\mathcal{F}$ decreases, the tube relaxes to a cylindrical shape more rapidly (over shorter length scales) from the contact point [cf. (3)]. In the limit $\mathcal{F} \to 0$ a corner forms at the ring of intersection between the sphere and the tube ($r = 1, z = z_i = \sqrt{R_0^2 - 1}$), as shown Fig. 3(a). In Fig. 3(b) we compare the predictions of our theory with experimental profiles for $R_0/a = 1.95$ and two dimensionless forces ($\mathcal{F} = 0.001$ and $\mathcal{F} = 0.5$), finding excellent agreement. Figure 3(a) also shows that stretching the tube lowers its contact area with the intruder. This is quantified in Fig. 3(c), where the position of the contact line z_c [obtained by solving (4)] relative to its unstretched value z_i is plotted as a function of $\mathcal{F}$. Analyzing (4) for $\delta_0 = R_0 - 1 \ll 1$ and $\mathcal{F} \ll 1$ shows that $z_i - z_c \sim \mathcal{F}^{1/2}$, up to corrections involving δ_0 [Fig. 3(c)].

The experimentally observed exponential decay of the radial displacement with the deformed arclength, $u_r - u_r^\infty \propto \exp\{-\lambda(S - S_c)\}$, is recovered by our numerical solutions (symbols in Fig. 2). The slope of an experimental or theoretical curve on this plot defines the decay constant λ for a given $\mathcal{F}$. The extracted λ values, representing (dimensionless) inverse decay lengths, are plotted against $\mathcal{F}$ in Fig. 4. Experimental decay exponents are shown for three different spherical intruder radii $R_0/a = 1.46$ (squares), 1.95 (circles), and 2.44 (diamonds) and are in good agreement with numerical results (solid curve) without fitting parameters.

Interestingly, our numerical results are insensitive to the intruder radius; calculated curves in Fig. 4 for different R_0/a are essentially identical. This is understood from the relation between the deformed and the undeformed coordinates: at large distances from the intruder, $u_r'(s) \ll u_z'(s) \sim \mathcal{F}$, which leads to the asymptotic result $S - S_c \sim (1 + \mathcal{F})(s - s_c)$. We note that the $(1 + \mathcal{F})$ is simply the stretch of the "bare" tube without an intruder. Substituting this relationship into (3a) identifies the universal decay exponent

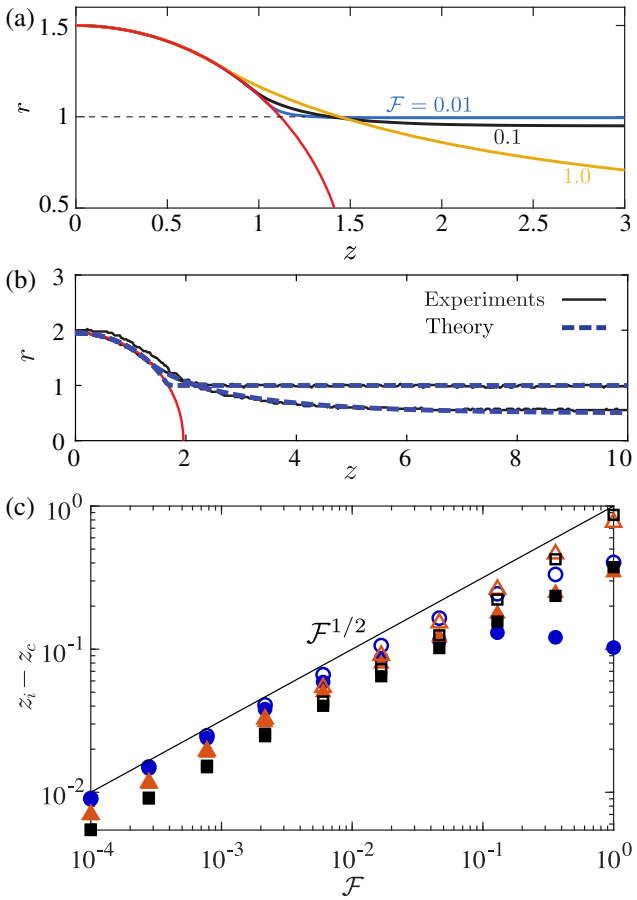

FIG. 3. (a) Theoretical prediction of the tube shape for different stretches $\mathcal{F}$ with $\nu = 1/2$ and a spherical intruder with $R_0/a = 1.5$. As $\mathcal{F}$ increases, the tube relaxes more gradually to a cylindrical shape, while the size of the contact region shrinks. The curvature at the contact point diverges as $\mathcal{F}^{-1/2}$. The dashed line indicates the undeformed shape of the tube. (b) Theoretical prediction (in dashed blue lines) and experimental tube shape (in solid black lines) for $R_0/a = 1.95$ and a small ($\mathcal{F} = 0.001$) and large ($\mathcal{F} = 0.5$) dimensionless stretching force. (c) Deviation of the contact length z_c from its no-stretch value z_i as a function of the applied stretching force $\mathcal{F}$. Symbols are numerical results for spherical intruders of different radii [$R_0 = 1.1$ (circles); $R_0 = 1.5$ (triangles); $R_0 = 2.0$ (squares)] and with different Poisson's ratio [$\nu = 0.5$ (filled); $\nu = 0$ (open)].

$$\lambda \approx \frac{1}{(1+\mathcal{F})\sqrt{\mathcal{F}}} = \frac{\sqrt{2\pi Eab/F}}{1 + F/(2\pi Eab)}. \tag{5}$$

The dimensional decay length is a/λ, which for small forces yields the length scale $\sqrt{Fa/(Eb)}$. The above result, plotted in Fig. 4 as a dashed curve, is practically indistinguishable from our numerical results for spherical intruders. Equation (5) also predicts insensitivity to the intruder size, shape, and the Poisson ratio of the material. All of these predictions are verified by numerical solutions for spheroids of a different aspect ratio and for different values of ν. In all cases, the computed results for λ are

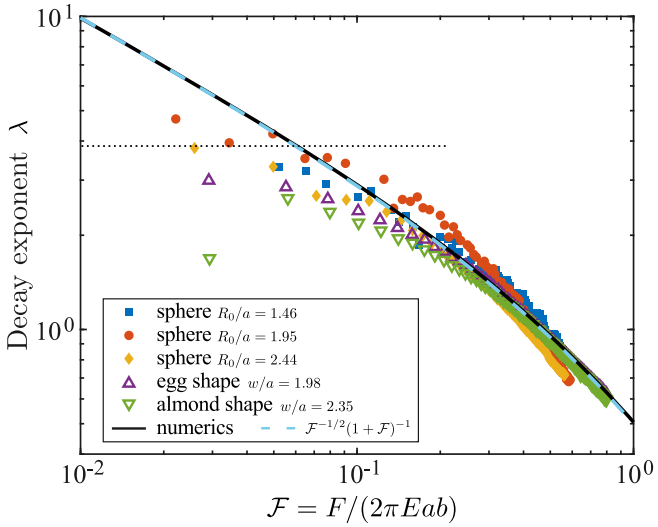

FIG. 4. Decay exponent λ vs $\mathcal{F}$ for spherical intruders with radius $R_0/a = 1.46$ (squares), 1.95 (circles), and 2.44 (diamonds), (axisymmetric) egg-shaped intruders ($\triangle$) with a half-width $w/a = 1.96$ and (asymmetric) almond-shaped intruders ($\triangledown$) with $w/a = 2.35$. Numerical results for spheres (solid curves; $\nu = 1/2$, R_0 matched with experiments) are insensitive to changes in intruder shape and size, and are in good agreement with the data. Both the experimental and the numerical results collapse onto the theoretical result (5) [dashed curve]. The horizontal dotted line at $\lambda = (\sqrt{2}\beta)^{-1} \approx 3.9$ corresponds to the bending-dominated limit with $\mathcal{F} \to 0$.

virtually identical to each other and to (5), even as z_c depends on both $R(z)$ and ν [cf. Fig. 3(c)].

The robustness of (5) is further confirmed by experiments with nonspherical intruders. Among others, these include ovoid shapes that break z symmetry and almond shapes that also break axisymmetry. Measured decay exponents for these shapes (maximal half-widths w) are plotted in Fig. 4 and collapse onto the universal curve (5) with no adjustable parameters; other shapes are shown in Supplemental Material [24]. For intruders above a certain size (typically $R_0/a \gtrsim 3$), the measured λ deviates from our theory by an $O(1)$ prefactor, although the qualitative dependence on $\mathcal{F}$ remains unchanged. This is attributed to the nonlinear response of the latex sheet to large [i.e., $O(1)$] strains (see Supplemental Material [24]).

At very small $\mathcal{F}$, the finite bending stiffness $B = [Eb^3/12(1-\nu^2)]$ of the tube comes into play. Including a bending traction $\sigma_b \approx Bu_r''''(s)\mathbf{e}_r$ in (1) [13] adds a term $\beta^4 u_r''''$ to the right side of (2a), where $\beta = [(b/a)^2/12(1-\nu^2)]^{1/4}$. In the limit $\mathcal{F} \to 0$, curvature around contact is regularized by a balance between bending and hoop stresses, giving $u_r \propto \exp\{-\sqrt{\pm i}(s-s_c)/\beta\}$ and identifying $\lambda \approx (\sqrt{2}\beta)^{-1}$. This gives $\lambda \approx 3.9$ for our experimental parameters, consistent with our measurements at small $\mathcal{F}$ (cf. Fig. 4), though we caution that the data are sensitive to noise in this limit. Axial strains dominate

bending in setting the curvature for $\sqrt{\mathcal{F}} \gtrsim \beta$ (i.e., $F \gtrsim Eb^2$), corresponding to a linear strain $\gtrsim O(b/a)$. Thus, a small amount of axial strain suffices to overwhelm bending as the dominant physical mechanism limiting out-of-plane curvature.

The features discussed here arise generically due to the curved cylinder geometry subject to an applied axial stretch and geometric constraints that include (but are not limited to) contacts with enclosed objects. Such stretching-generated curvatures may be observable at the microscale and could be used to infer the mechanics of membrane tethers [6] and microtubules [18,25] by varying the applied tensile load. At larger scales, the modification of radial geometry by axial forces are also likely to have an influence on the movement of fluid and enclosed solid objects through soft tubes [19,20] due to peristalsis or external forces. The ability to produce out-of-plane curvatures with externally applied in-plane tensile strains may also provide a new handle to dynamically tune the geometry of engineered soft surfaces.

In conclusion, by considering the elastic trapping of objects inside a cylindrical tube of radius a and thickness b, we have investigated a mechanism of curvature regularization in soft curved systems that is produced by in-plane tension. From the competition between hoop stress and longitudinal stretching arises a novel length scale $\sqrt{Fa/(Eb)}$, which *decreases* with increasing sheet thickness, opposite the usual elastic cut-off scale [1], which smooths the sheet with increasing thickness. The geometric underpinnings of this curvature production mechanism suggests its broad applicability to naturally curved soft shells under axial strains.

We are grateful to Dominic Vella for his insightful comments. This work was initiated while B. R. was affiliated with Princeton University. E. J.-P. was partially supported by the NSF through the Princeton University Materials Research Science and Engineering Center DMR-142054. J. E. acknowledges support by the Leverhulme Trust through International Academic Fellowship IAF-2017-010. He benefitted from inspiring conversations with Howard Stone and his group, during an unforgettable sabbatical year at Princeton.

B. R. and J. M. contributed equally to this work.

*bhargav@engr.ucr.edu
†majge@bristol.ac.uk

[1] T. A. Witten, Rev. Mod. Phys. **79**, 643 (2007).
[2] E. Cerda and L. Mahadevan, Phys. Rev. Lett. **90**, 074302 (2003).
[3] M. Taffetani and D. Vella, Phil. Trans. R. Soc. A **375**, 20160330 (2017).
[4] J. Huang, M. Juszkiewicz, W. H. De Jeu, E. Cerda, T. Emrick, N. Menon, and T. P. Russell, Science **317**, 650 (2007).
[5] B. Davidovitch, R. D. Schroll, D. Vella, M. Adda-Bedia, and E. A. Cerda, Proc. Natl. Acad. Sci. U.S.A. **108**, 18227 (2011).
[6] T. R. Powers, G. Huber, and R. E. Goldstein, Phys. Rev. E **65**, 041901 (2002).
[7] D. Vella, A. Ajdari, A. Vaziri, and A. Boudaoud, Phys. Rev. Lett. **107**, 174301 (2011).
[8] J. Huang, B. Davidovitch, C. D. Santangelo, T. P. Russell, and N. Menon, Phys. Rev. Lett. **105**, 038302 (2010).
[9] L. Pocivavsek, R. Dellsy, A. Kern, S. Johnson, B. Lin, K. Y. C. Lee, and E. Cerda, Science **320**, 912 (2008).
[10] T. von Karman and H.-S. Tsien, J. Aeronaut. Sci. **8**, 303 (1941).
[11] A. V. Pogorelov, in *Translations of Mathematical Monographs* (American Mathematical Society, 1988), Vol. 72, https://doi.org/10.1090/mmono/072.
[12] S. Knoche and J. Kierfeld, Eur. Phys. J. E **37**, 62 (2014).
[13] B. Audoly and Y. Pomeau, *Elasticity and Geometry: From Hair Curls to the Non-linear Response of Shells* (Oxford University Press, New York, 2010).
[14] H. S. Seung and D. R. Nelson, Phys. Rev. A **38**, 1005 (1988).
[15] R. Sknepnek, G. Vernizzi, and M. O. de la Cruz, Soft Matter **8**, 636 (2012).
[16] S. Kim and S. Hilgenfeldt, Soft Matter **11**, 8920 (2015).
[17] L. Mahadevan, A. Vaziri, and M. Das, Europhys. Lett. **77**, 40003 (2007).
[18] P. J. de Pablo, I. A. T. Schaap, F. C. MacKintosh, and C. F. Schmidt, Phys. Rev. Lett. **91**, 098101 (2003).
[19] M. J. Lighthill, J. Fluid Mech. **34**, 113 (1968).
[20] D. Takagi and N. J. Balmforth, J. Fluid Mech. **672**, 219 (2011).
[21] A. Léger and B. Miara, J. Elastoplast. **131**, 19 (2018).
[22] L. D. Landau and E. M. Lifshitz, in *Theory of Elasticity, Course of Theoretical Physics* Vol. 7 (Elsevier, New York, 1986).
[23] J. Eggers and E. Villermaux, Rep. Prog. Phys. **71**, 036601 (2008).
[24] See Supplemental Material at http://link.aps.org/supplemental/10.1103/PhysRevLett.123.168002 for additional theoretical and experimental details.
[25] A. Kis, S. Kasas, B. Babić, A. J. Kulik, W. Benoît, G. A. D. Briggs, C. Schönenberger, S. Catsicas, and L. Forró, Phys. Rev. Lett. **89**, 248101 (2002).

Supplementary Material: Curvature regularization near contacts with stretched elastic tubes

Bhargav Rallabandi,[1,*] Joel Marthelot,[2] Etienne Jambon-Puillet,[2] P.-T. Brun,[2] and Jens Eggers[3,†]

[1] *Department of Mechanical Engineering, University of California, Riverside, California 92521, USA*
[2] *Department of Chemical and Biological Engineering, Princeton University, Princeton, New Jersey 08544, USA*
[3] *School of Mathematics, University of Bristol, University Walk, Bristol BS8 1 TW, UK*

(Dated: September 19, 2019)

JUMP CONDITIONS AT CONTACT LINES

For a line density of contact force $\mathbf{f}_c$ acting at the contact lines $s = s_c$, the condition at s_c, obtained from a variation of the membrane stretching energy (see [1] for details) has the form

$$[[N_s\mathbf{t}]]_{s_c} + \mathbf{f}_c = \mathbf{0}, \tag{S.1}$$

where $[[f]]_{s_c} = f(s_c^+) - f(s_c^-)$ denotes the jump around s_c. In the absence of friction, $\mathbf{f}_c$ must be directed along the common normal to both the intruder and the tube surface as it is a contact force. This lets us conclude continuity of the tangent vector and the normal stress across the contact lines, $[[\mathbf{t}]] = \mathbf{0}$ and $[[N_s]]_{s_c} = 0$. This is equivalent to continuity of the displacement (no cuts) and its gradient: $[[u_r]]_{s_c} = [[u_z]]_{s_c} = [[u_r']]_{s_c} = [[u_z']]_{s_c} = 0$. Using Eqs. (2) and (3) of the main text [recognizing that $C = -\sqrt{\mathcal{F}}u_r'(s_c)$], these conditions are more conveniently expressed in terms of dimensionless variables as

$$u_r'\sqrt{\mathcal{F}} + u_r + \nu\mathcal{F} = 0 \quad \text{at} \quad s = s_c. \tag{S.2a}$$

$$\left(u_z' + \frac{1}{2}(u_r')^2 + \nu u_r\right) = (1-\nu^2)\mathcal{F} \quad \text{at} \quad s = s_c, \tag{S.2b}$$

where the second condition is identical to the continuity of N_s. Defining $\delta(z) = R(z) - 1$, the geometric constraint in the contact region and its derivatives,

$$u_r(s) = \delta(s + u_z(s)), \quad u_r' = (1 + u_z')\delta' \quad \text{and} \quad u_r'' = (1 + u_z')^2\delta'' + u_z''\delta', \tag{S.3}$$

can be used to eliminate u_r and its derivatives in favor of δ, u_z, and their derivatives. Thus, (S.2a) can be expressed as

$$u_z' = -1 - \frac{1}{\sqrt{\mathcal{F}}}\frac{\delta + \nu\mathcal{F}}{\delta'} \quad \text{at} \quad s = s_c^-, \tag{S.4}$$

which on substituting into (S.2b) (along with (S.3)) yields Eq. (4) of the main text. Solving this equation (numerically) yields the axial location z_c of the contact line. This value can then be substituted into (S.4) to obtain $u_z'(s_c)$, enforcing a boundary condition on the solution at the contact line.

STRESS BALANCE IN THE CONTACT REGION

We consider the stress balance (Eq. (1) of the main text) with the contact stress $\boldsymbol{\sigma} = p_c(s)\mathbf{n}$. Taking an inner product of this equation with the tangent $\mathbf{t}$ eliminates the unknown pressure $p_c(s)$. In terms of the dimensionless displacement field, the resulting equation is

$$\left(u_r''u_r' + \left(1 + (u_r')^2\right)\frac{\mathrm{d}}{\mathrm{d}s}\right)\left(u_z' + \frac{1}{2}(u_r')^2 + \nu u_r\right) - \left(u_r + \nu\left(u_z' + \frac{1}{2}(u_r')^2\right)\right)u_r' = 0, \tag{S.5}$$

which is valid throughout the contact region. As before, we use the geometric conditions (S.3) to write u_r and its derivatives in terms of u_z and its derivatives. This yields a second-order nonlinear ordinary differential equation involving u_z'', u_z', u_z, s and the known functions δ, δ' and δ''. We integrate this equation numerically with the condition $u_z(0) = 0$ (symmetry) and the contact condition (S.4). Here, a shooting algorithm is employed to solve the two-point boundary value problem: successively improved guesses for $u_z'(0)$ are used until the contact condition (S.4) is met to a tolerance of within 10^{-6}. On solving for $u_z(s)$, $u_r(s)$ is evaluated through the kinematic condition (S.3).

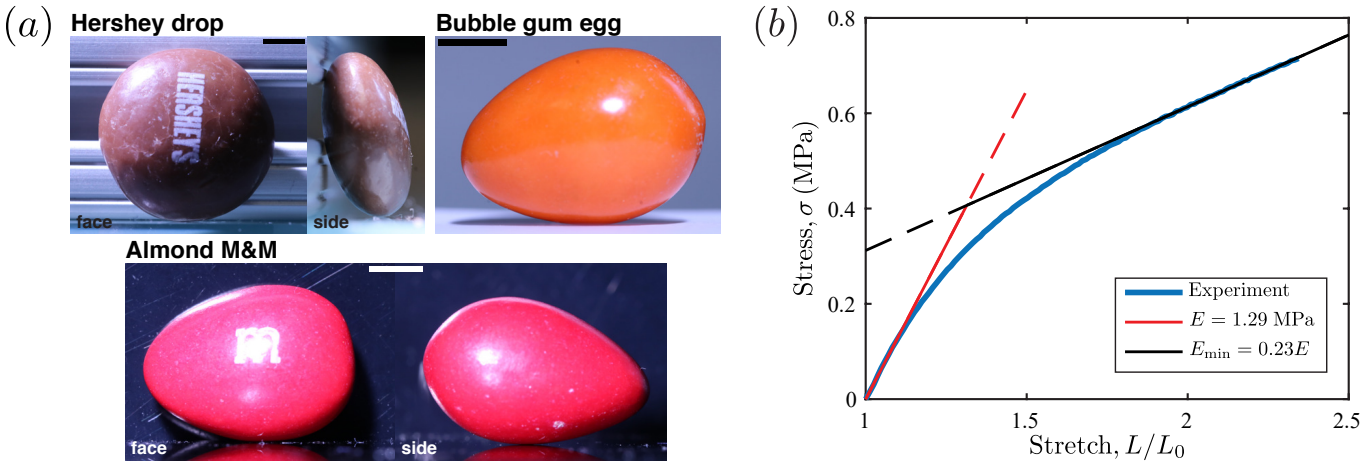

FIG. S.1. (a) Pictures of the non-spherical intruders used. Scale bars are 5 mm. (b) Engineering stress vs stretch curve for empty balloons.

EXPERIMENTAL DETAILS

We use ball bearings as spherical intruders and candies as non-spherical intruders (see Fig. S.1a). Hershey drops have an oblate spheroidal shape (aspect ratio= 2), bubble gum eggs are ovoid (axisymmetric), almond M&M's have no symmetries. Our elastic tubes are commercial latex balloons (Nexci animal balloons). Although cylindrical once inflated, they have an ellipsoidal rest cross-section (eccentricity≈ 0.65) with a perimeter-based equivalent radius of $a = 3.25$ mm and a constant thickness $b = 320$ μm. They are hyperelastic with a Young's modulus of $E = 1.29$ MPa at low strain measured through uniaxial tension (see Fig. S.1b).

The balloons are first pre-inflated once before putting and centering the intruder manually. The balloon ends are cut and clamped in a vertical orientation in the tensile tester (Instron) with rigid tubes inserted at the ends to avoid deformations by the clamp. We then pull on them up to 80 cm ($\approx 250\%$ stretch) while recording the force and the balloon shape around the intruder with a high resolution camera following the intruder on a motorized translation stage.

The images are then processed with Matlab. The intruder position is detected through circle fitting for spherical intruders and through image correlation for non-spherical intruders (see Movie S1). The displacement u_r and arclength S are then measured on the four regions not in contact and the decay length is extracted by fitting $u_r = A\exp\left[-\lambda\left(S - S_c\right)\right] + u_r^\infty$ to the data. In addition to A and λ we also fitted u_r^∞ within the experimental uncertainties (≈ 0.05).

We checked the influence of the elliptical rest cross-section of the tubes by repeating an experiment while slightly inflating the balloon before stretching it so that it recovers a circular cross section, and by performing the image analysis on both the thin and wide side. No significant differences in the value of λ were found. Because the weight of the large ball bearings pre-stretches the upper side of the balloon before the experiment starts, we extract λ from the lower part of the image only. We further checked that we obtained the same value of λ by repeating the experiment for $R_0/a = 3.9$ with a plastic ball of negligible weight. For candies, the values of λ on the upper and lower sides are similar and we averaged them.

LARGE INTRUDERS

The numerical predictions for λ are found to be independent of intruder size. This holds experimentally as well up to a size of roughly three time the balloon rest radius. Fig. S.2a shows the decay exponent for all our experiments, including large intruders. For the two largest spheres ($R_0/a = 3.9$, $R_0/a = 4.88$) and the axisymmetric Hershey drop we observe a lowering of the decay exponent that we attribute to material nonlinearity. Indeed, as shown in Fig. S.1b the rubber of the balloon is hyperelastic and we observe strain softening in uniaxial tension above a stretch of $\approx$1.3.

Experimentally, reducing the Young's modulus E by a factor 0.65 in the calculation of $\mathcal{F}$ for the $R_0/a = 3.9$, 4.88 experiments is able to collapse all the data on the theory (see Fig. S.2b), except for the largest sphere at low $\mathcal{F}$. Note that in our experiments with intruders, the stretch is non-uniform and biaxial, with a component due to the

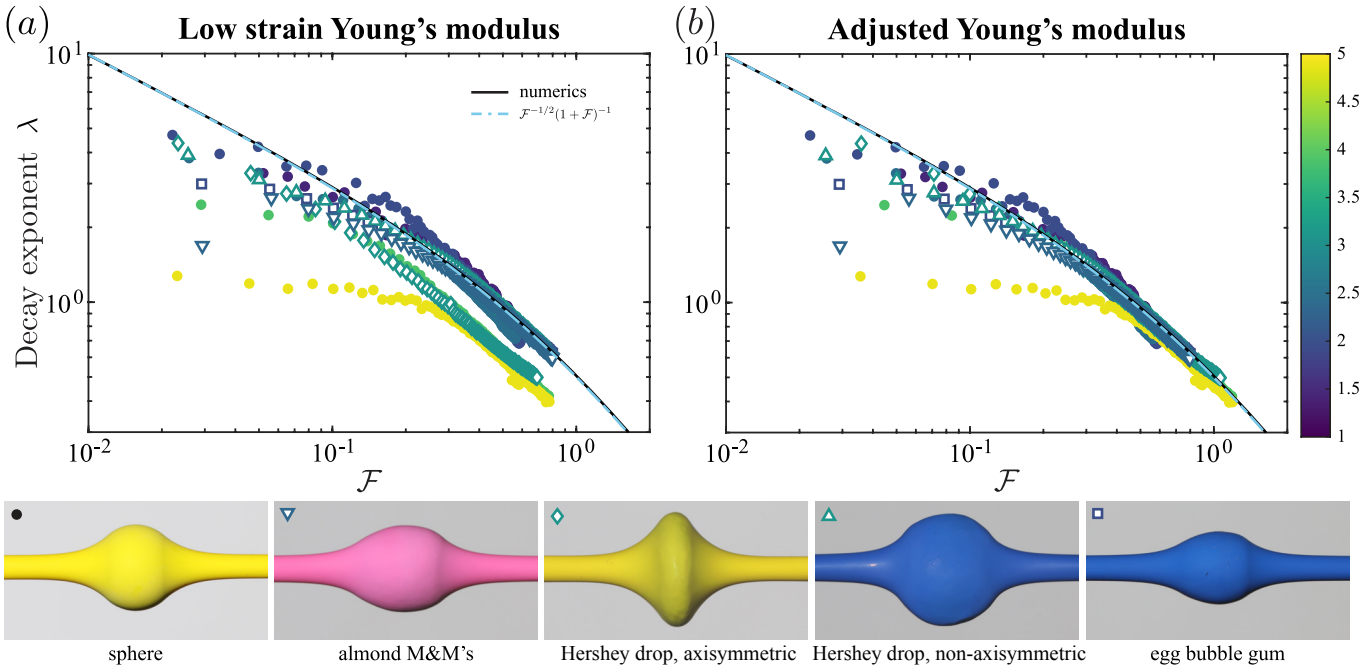

FIG. S.2. (a) Decay exponent λ as a function of the dimensionless force $\mathcal{F} = F/(2\pi Eab)$ for all our experiments, using the low strain Young's modulus. Symbols code the intruder type and the color their dimensionless size (using the largest dimension for non-spherical intruders). (b) Same data with the Young's modulus multiplied by 0.65 for the large spheres ($R_0/a = 3.9$, $R_0/a = 4.88$) and the axisymmetrically-oriented Hershey drop ($w/a = 3.1$).

intruder and another from the external stretching. A direct quantitative correspondence between the uniaxial stretch-strain relationship and the softening induced by intruder size requires a detailed modeling of the nonlinear material response and is not pursued here. The influence of biaxiality is further illustrated by the fact that depending on its orientation (axisymmetric vs non-axisymmetric), the Hershey drop either does or does not probe the material nonlinearity, showing that the hoop and axial stretch play distinct roles in determining λ.

* bhargav@engr.ucr.edu
† majge@bristol.ac.uk

[1] B. Audoly and Y. Pomeau, *Elasticity and Geometry: From Hair Curls to the Non-linear Response of Shells* (Oxford University Press, 2010).